PAPER

Purified nonlinear guided waves through a metamaterial filter for inspection of material microstructural changes

View the article online for updates and enhancements.

Purified nonlinear guided waves through a metamaterial filter for inspection of material microstructural changes

Shengbo Shan[1,2], **Fuzhen Wen**[1,3,4] **and Li Cheng**[1,3,4,*]

[1] Department of Mechanical Engineering, The Hong Kong Polytechnic University, Kowloon, Hong Kong
[2] School of Aerospace Engineering and Applied Mechanics, Tongji University, Shanghai 200092, People's Republic of China
[3] The Hong Kong Polytechnic University Shenzhen Research Institute, Shenzhen 518057, People's Republic of China
[4] Hong Kong Branch of National Rail Transit Electrification and Automation Engineering Technology Research Center, The Hong Kong Polytechnic University, Kowloon, Hong Kong

E-mail: li.cheng@polyu.edu.hk

Abstract

Nonlinear guided waves (NGWs) exhibit extraordinary sensitivity to microstructural changes in materials which are often considered as damage precursors in many structural health monitoring (SHM) applications. However, these changes are usually very small at the microstructural level, thus generating weak nonlinear wave components which are prone to or even overwhelmed by other deceptive and non-damage-related nonlinear sources present in a monitoring system. This may jeopardize the practical implementation of the NGW-based SHM methodology. To tackle this problem, this paper proposes a metamaterial filter (meta-filter (MF)), in the form of a patch to be surface-mounted over the structure under inspection. The MF is designed to purify the probing waves during propagation before reaching the inspection area through tactical elimination of non-damage-related nonlinear components from the actuation. Considering different bonding conditions and the lattice symmetry of the MF, two types of bandgaps, corresponding to Bragg scattering and local resonances, alongside their respective band properties are analyzed. Time-domain finite element simulations are carried out to assess the efficacy of the MF in terms of wave purification in the context of SHM, supported by experimental validations. The designed MF is deployed in an aluminum strip to detect the material microstructural changes induced by a thermal ageing treatment. Results demonstrate the designed MF significantly enhances the detection ability of NGW-based SHM system. Both locally resonant and Bragg bandgaps can, in principle, be used for wave purification. While the former requires precise control of the bonding quality of the MF, the latter relies on symmetrical installation of the MF to ensure a reasonably wide wave filtering range. Considering variability factors in the implementation of the MF and better immunity to the nonlinearity of the bonding layers, preference is given to Bragg bandgap for NGW-based SHM applications.

Keywords: nonlinear guided waves, metamaterial, Bragg scattering, local resonance, structural health monitoring

(Some figures may appear in color only in the online journal)

---

* Author to whom any correspondence should be addressed.

1

1. Introduction

Structural/material damage in engineering structures, which evolves through different stages starting from microstructural defects to a more observable stage of macro defects, may degenerate to catastrophic structural failure without timely awareness and action. To reduce such risks, structural health monitoring (SHM) based on guided waves emerges as a promising technique to deliver online and real-time inspection capabilities [1, 2]. Conventional linear-guided-wave-based methods have shown proven effectiveness for macro defect detection based on wave scattering features [3, 4]. However, they can hardly cope with the detection of incipient damage related to microstructural changes, which is of paramount importance for early decision making in engineering applications [5, 6].

When probing guided waves propagate and interact with microstructural defects like lattice anomalies, dislocations, micro-cracks etc, energy can be shifted from the fundamental frequency to other frequencies to generate nonlinear components, exemplified by the second harmonic generation [7–9]. As a result, nonlinear-guided-wave-based SHM (NGW-SHM) methods inherently exhibit higher sensitivity to microstructural defect-related incipient damage than their linear counterparts do, as demonstrated on various types of incipient damage under laboratory conditions [10–13]. For example, Yang *et al* investigated the second harmonic generation by both primary S0 and A0 Lamb waves to detect the contact acoustic nonlinearity induced by a fatigue crack in a 5005-H34 aluminum plate [10]. Pruell and Kim used the primary S1-second harmonic S2 Lamb wave mode pair to characterize the extent of the plastic deformation in 1010-H14 aluminum plates [11]. Deng and Pei monitored the fatigue process of an aluminum sheet with the second harmonic Lamb waves (primary A2-second harmonic S4 mode pair), demonstrating their high sensitivity to incipient fatigue damage [12]. In addition, the primary S0-second harmonic S0 Lamb wave mode pair was successfully used to detect thermal-ageing-induced microstructural changes in 2024-T3 aluminum plates in our previous work [13].

In practical applications, incipient-damage-induced higher harmonic wave components are usually weak due to the minor material changes in the microstructural level. A precise and reliable extraction of the damage-related nonlinear wave components is a prerequisite to guarantee the success of NGW-SHM techniques. Despite the aforementioned laboratory demonstrations, the development of off-the-shelf and reliable NGW-SHM techniques for material microstructural change detection is still in an embryonic stage. One of the critical issues is tied with numerous deceptive nonlinear wave components originating from non-damage-related nonlinear sources mainly from the actuation region. In particular, a high input level is usually required in any NGW-SHM system to guarantee the strong excitation of fundamental waves for further higher harmonic generation when interacting with the damage. The unavoidable presence of these deceptive nonlinear components might overwhelm the damage-induced nonlinear waves [14, 15]. Taking a typical NGW-SHM system illustrated in figure 1 as an example, the nonlinear responses captured by a sensor may result from: (a) wave actuating part including actuators, bonding layers and associated electric instruments; (b) waveguide under inspection and structural/material damage such as material nonlinearity and breathing cracks; (c) sensing part including sensors, the corresponding bonding layers and data acquisition modules. Compared with the sensing part, the wave actuating part is more critical due to the higher level of the flowing energy [14], which requires proper mitigation so that the deceptive nonlinear components due to the actuation can be minimized before the waves reach the inspection area.

The problem may potentially be tackled on two fronts: (a) a best possible system design through proper parameter setting and (b) an effective manipulation of different nonlinear wave components. The former has been partially addressed in our previous work [13], which has, to a certain extent, allowed reducing the non-damage-related adhesive nonlinearity with the help of a theoretical model. However, the model was unable to consider all possible nonlinear sources and the determined optimal probing frequency was restricted to some particular values. This forms the main motivation of the present work. The basic idea is to embrace the concept of phononic crystals and metamaterials to achieve tactical wave manipulations. Specifically, it is expected that a proper metamaterial device is designed and customized to purify the guided waves emitted from the actuation area by eliminating the deceptive nonlinear components before they reach the inspection area.

Metamaterials, artificial functional media structured on the subwavelength scale, have shown great promise for elastic wave manipulation [16–20]. With properly tailored unit cells and distribution pattern, metamaterials allow constructing abundant combinations of effective material parameters, thus leading to many applications such as wave/vibration attenuation [21], mode conversion [16, 22] and wave steering [23], etc. Despite the extensive works on metamaterials, mainly in the context of physics and phenomenon discovery, their exploration in SHM is still scarce. Some relevant efforts include the design of a metamaterial device for the second harmonic response filtering [24] and selective mode transmission [25], both mainly focusing on the wave propagation characteristics without any specific focus on damage inspection. More closely related to the present topic, Tian *et al* presented an interesting work by using the local resonance-based metamaterial concept to eliminate the second harmonic responses induced by the non-damaged-related sources and applied it to the detection of a breathing crack [15]. The damage case considered in that work (a rather localized crack) is different from the material microstructural changes to be considered in the present paper. The material microstructural changes should be weak in level and distributed within an area, which would give rise to energy shift and accumulation along the wave propagation. Presumably, this is even more demanding in terms of wave manipulation. In addition, most phononic crystal components reported in the literature need to be independently bonded on the structure to form a lattice [15, 25], which requires a miscellaneous installation and poses harsh
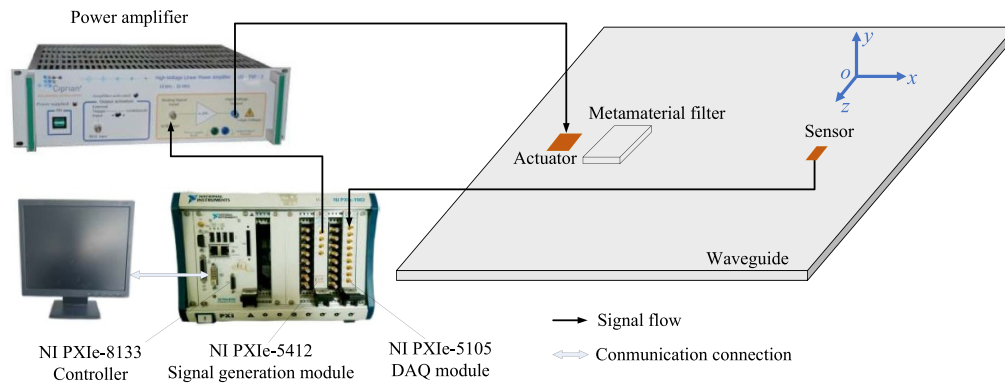
Figure 1. Sketch of a typical NGW-SHM system and the metamaterial filter installation.

demand in terms of installation quality. Moreover, it can be surmised that the material nonlinear properties from the adhesive for bonding these phononic crystals might pose extra challenges to SHM applications.

In this work, a metamaterial filter, called meta-filter (MF) in short, is designed and investigated. Taking the form of a lead patch, a pair of MFs will be bonded on both the top and bottom surfaces of a thin-walled structure through adhesive bonding layers for SHM between the actuation and inspection areas. By examining the band structure of the MF assembly, the influences of the bonding conditions and the lattice symmetry of the MF on the bandgaps are analyzed to show the customized wave filtering capability alongside the underlying mechanisms. Time-domain finite element studies are carried out to validate the efficacy of the designed MF in terms of wave filtering. The material nonlinearity of the adhesive in the MF assembly is highlighted to show its influence on the nonlinear wave purifying efficiency. Experiments are finally conducted in the context of material microstructural change inspection, in which the second harmonic Lamb waves are purified by the MF and applied to detect the thermal-ageing-induced material changes in an aluminum strip, as a proof-of-concept demonstration.

2. Metamaterial filter design and analyses

Previous works have confirmed the quasi-cumulative behavior of the second harmonic S0 mode Lamb waves with respect to propagating distance in a wide low-frequency range and their effective use for material microstructural change inspection [13, 26]. This work follows the same logic and also focuses on the low frequency range (typically below 300 kHz for a 2 mm thick aluminum plate) where the selection of the excitation frequency is flexible for the S0 wave generation.

An MF is designed to mitigate the deceptive nonlinear components generated in the actuation area in order to discern the nonlinear waves induced by material changes in the inspection area. The MF is to be installed in the vicinity of the actuator over the structure under inspection to purify the NGWs as sketched in figure 1. In the context of SHM, three requirements are hatched out for the design of the MF: (a) to conceive an auxiliary device without damaging the structure

under inspection; (b) to filter out non-damage-related nonlinear waves generated by the instrument, actuator, and adhesive layer in the actuating area; and (c) to allow sufficiently strong linear probing waves to reach the inspection area so as to entail effective generation of the damage-related NGWs.

Embracing the concept of bandgap generation in periodic phononic crystals, an MF, composed of a series of periodically arranged T-shaped lead patch, is designed to be surface-mounted on each side of an aluminum plate through adhesive layers as illustrated in figure 2(a). Some salient points related to the MF design are summarized as follows. The proposed design starts with a unit cell. Specifically, the lattice constant a (the length of the unit cell) is first determined as 4 mm which, in the present case, is in the sub-wavelength range with respect to the Lamb wave wavelength under consideration. For practical installation, a base is used to connect the block scatterers, which results in the T-shaped design of the lead patch in the unit cell. Since the S0 mode Lamb waves are used for SHM applications, the patches are symmetrically bonded on the aluminum plate under inspection. The width and height of the block are carefully tuned to produce proper band structures to ensure the effective generation of band gaps within which waves are prohibited to propagate. As a result, the designed unit cell contains a pair of T-shaped lead blocks, a plate segment and the bonding layers in-between as shown in figure 2(b). The geometric parameters of the lead patches are listed in table 1. The thickness of the bonding layers is assumed to be 50 μm. Material parameters such as the mass density ρ, Young's modulus E, and Poisson's ratio v for the three components are tabulated in table 2. It is worth noting the nonlinear material elastic properties are not included in the band structure calculations.

The band structure of the MF assembly (unit cell) is calculated using COMSOL Multiphysics 5.4. A sufficiently refined meshing, shown in figure 2(b), is adopted to ensure the accuracy of the calculation. The periodicity across unit cells is introduced by applying the Bloch-Floquet boundary conditions on the left and right edges of the unit cell. By sweeping the wave number k and searching for frequencies f, the band structure is calculated and shown in figure 2(c). Two bandgaps (111–142 kHz for BG1, 193–222 kHz for BG2) are observed within which no Lamb waves can propagate.

(a)

(b)

(c)

(d)
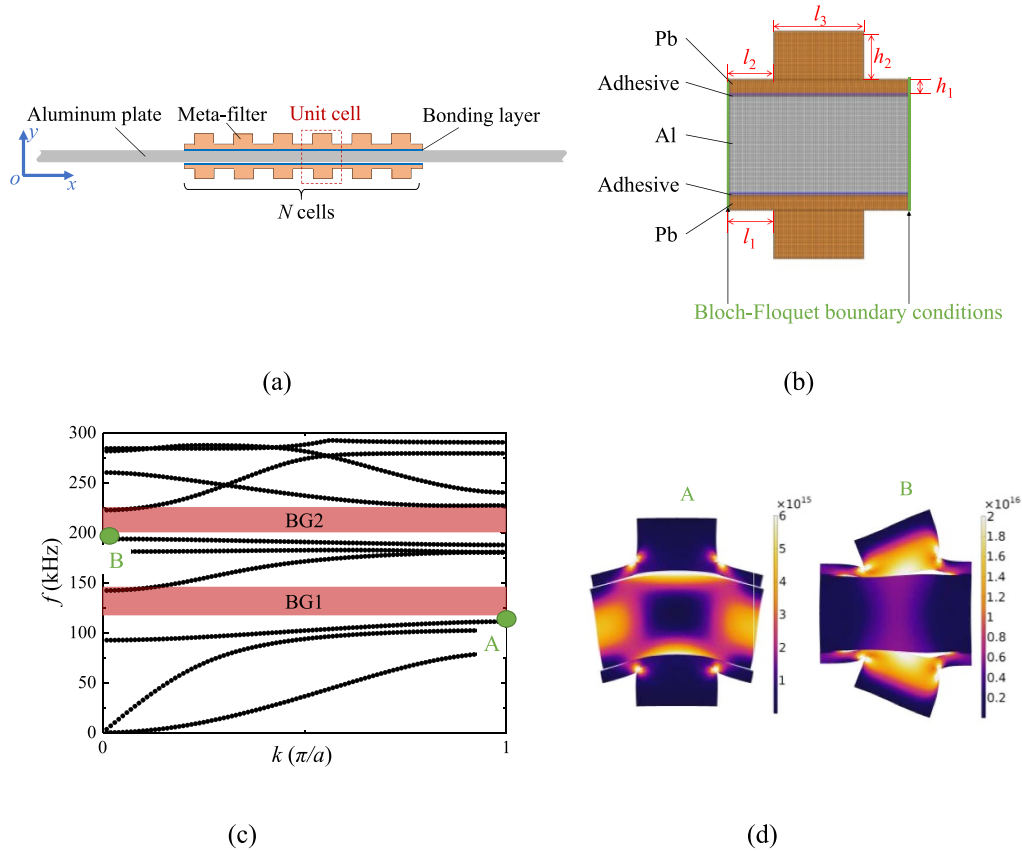
Figure 2. (a) Sketch of the MF assembly; (b) the unit cell of the MF assembly; (c) band structure of the designed MF assembly; (d) structural deformation at the cut-on frequencies of the two bandgaps with the color denoting the stored energy density.

Table 1. Geometric parameters of the lead patch (unit: mm).

h_1	h_2	l_1	l_2	l_3
0.3	1	1	1	2

As mentioned above, the SHM approach, based on low-frequency second harmonic S0 mode waves, does not need to target particular frequency because it allows a very flexible choice of the probing frequency for the inspection of material microstructural changes. Once the band structure is achieved with the designed MF, we can simply select a fundamental frequency within the passband while ensuring that its second harmonic frequency falls into the stopband. In this case, the linear waves can pass through the MF while the corresponding nonlinear waves can be eliminated. Therefore, the device can be utilized as a filter for the NGW-SHM applications.

The observed bandgaps are scrutinized to ascertain their wave filtering ability, the underlying generation mechanisms as well as the effects of some factors pertaining to implementation. The observed bandgaps can be examined from two mechanisms that are well established in the metamaterial community: local resonances [27–30] and Bragg scattering [30–32]. For the former, locally resonant elements sequester energy and prohibit wave propagation, thus leading

to significant wave attenuation along the propagation path. Therefore, local resonance bandgaps are strongly dependent on the resonant frequencies of the unit cells but less sensitive to the spatial periodicity of the resonant elements [29]. On the contrary, the Bragg bandgaps are the results of multiple waves scattering and interference between the periodically distributed elements. Spatial periodicities are either comparable to the wavelengths [30, 32], or smaller to achieve sub-wavelength performance. Based on the understanding, bandgaps observed in figure 2(c) are examined. Structural deformation of the unit cell at the cut-on frequencies of the two stopbands (marked by A and B in figure 2(c)) is depicted in figure 2(d) in terms of the stored energy density. Severe deformation occurs at the host structure at the cut-on frequency of the first bandgap (A) with little deformation of the lead blocks, drastically different from its counterpart of the second bandgap (B), for which structural deformation mainly occurs on the local lead bocks and the adhesive base. This indicates that the first bandgap is mainly caused by Bragg scattering while the second one by local resonance.

The influence of the lattice configurations on the bandgaps is then investigated to better understand the characteristics of the designed MF. Two key factors, pertaining to the practical installation of the MFs, are investigated, namely the lattice symmetry and the bonding thickness.

Table 2. Material parameters of aluminum, adhesive, and lead.

	ρ (kg m^{-3})	E (GPa)	v	$\bar{A}$ (GPa)	$\bar{B}$ (GPa)	$\bar{C}$ (GPa)
Aluminum	2700	70	0.33	−351.2	−140.4	−102.8
Adhesive	1080	1.31	0.4	−20.9	−8.3	−6.1
Lead	11 370	16	0.42	—	—	—
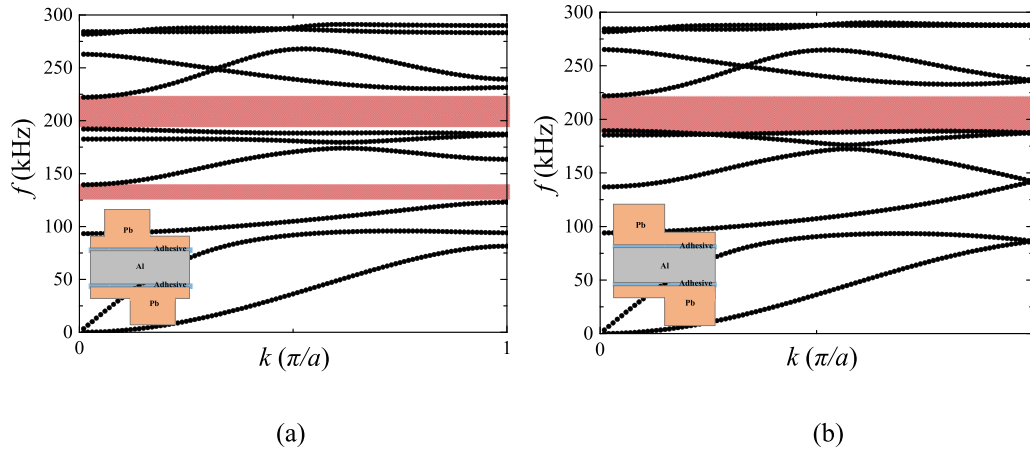
Figure 3. Band structures of the MF assembly with different block locations: (a) $l_1 = 1.5$ mm and $l_2 = 0.5$ mm; (b) $l_1 = 2$ mm and $l_2 = 0$ mm.

2.1. Lattice symmetry

The installation position of the MF patches is first altered to destroy the afore-assumed symmetry of the metamaterial lattice with respect to the mid-plane of the plate to mimic the possible misalignment of the MF patches during their practical installation. Two representative cases are presented by using different values of l_1 and l_2, defined in figure 2(b) and shown in figure 3. Specifically, we set l_1 and l_2 to 1.5 mm and 0.5 mm respectively for the case in figure 3(a) and 2 mm and 0 mm for the case in figure 3(b) to offset the lattice symmetry. Other geometric parameters are kept the same as those in the original case in table 1. By comparing the band structures shown in figures 2(c), 3(a) and (b), it is evident that the lattice symmetry has a significant influence on the first bandgap by narrowing it down but has a negligible impact on the second bandgap. This is consistent with the nature of the first band as described previously, since the altered spatial distribution of the MFs affects the wave interference of the scattering waves so that this Bragg bandgap is significantly impaired. On the contrary, the alteration in the MF position does not affect the mass and the stiffness of the unit cells so that their local resonance frequencies remain unchanged. As a result, the locally resonant bandgap remains unchanged by altering the lattice symmetry. From the SHM perspective, this means that locally resonant bandgaps are more robust to the misalignment of the MF patches.
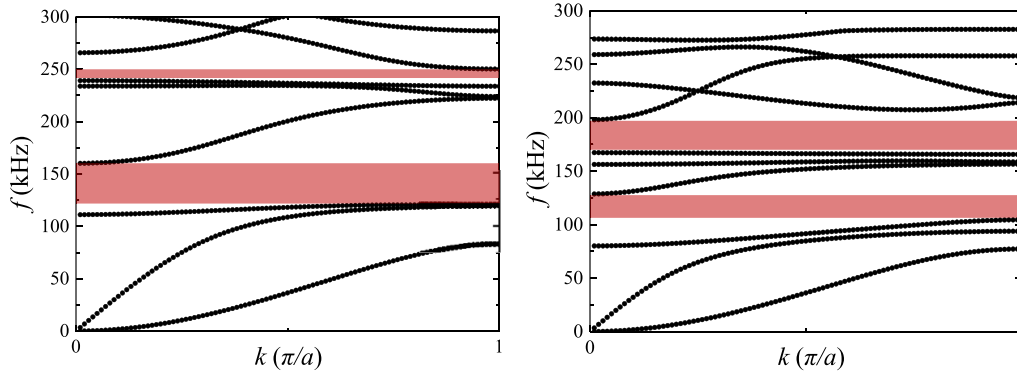
2.2. Bonding thickness

Effects of the bonding thickness of the adhesive on the band structure of the MF assembly are investigated. In practical applications, the thickness of the bonding layer is difficult to be precisely and consistently controlled, with a plausible range typically from 1 μm to 100 μm [33]. Therefore, two extreme cases, namely 1 μm and 100 μm, are examined. Similarly, other geometric parameters of the metamaterial lattices remain identical to those used in the original case. Corresponding band structures are shown in figures 4(a) and (b), respectively. Comparisons with the original case in figure 2(c) show that the bonding thickness affects significantly the locally resonant bandgap in terms of both its location and bandwidth, but only slightly the first Bragg bandgap. This is because the bonding thickness directly determines the stiffness of the local resonators (T-shaped block with the adhesive) so that the local resonance frequencies are affected when the bonding thickness changes.

To sum up, an MF is designed which shows promise for wave filtering owing to the creation of two bandgaps, which correspond to the Bragg scattering and local resonance mechanisms, respectively. The Bragg bandgap is sensitive to the MF installation in terms of lattice symmetry while the locally resonant one is more vulnerable to the variations in the bonding thickness. If the bonding thickness cannot be precisely and consistently controlled, the Bragg scattering induced bandgap is preferred to be used for wave filtering in practical applications. Misalignment of the MF installation, reflected by the loss of lattice symmetry, would reduce the bandwidth of the effective wave filtering.

3. Numerical validation of the designed metamaterial filter

A time-domain finite element model is developed using Abaqus considering a pair of symmetric lead zirconate titanate (PZT) actuators bonding on a 2 mm thick aluminum plate,

Figure 4. Band structures of the MF assembly with different bonding thicknesses: (a) 1 μm; (b) 100 μm.
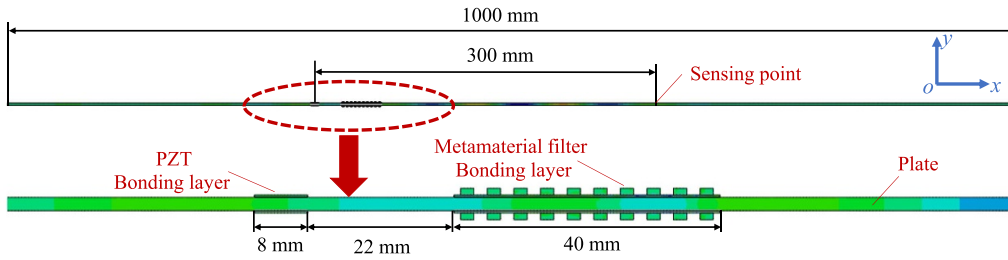
Figure 5. Physical model used in finite element analyses.

Table 3. Material parameters of PZT used in the FE model.

Mass density	Elastic constants		Piezoelectric constants[a]			Dielectric constants[a]	
ρ	E	v	$d_{2\,11}$	$d_{2\,22}$	$d_{1\,12}$	e_{11}	e_{22}
7650 kg m^{-3}	62 GPa	0.32	-210 pm V^{-1}	472 pm V^{-1}	758 pm V^{-1}	20.1 nF m^{-1}	18.9 nF m^{-1}

[a] Subscripts 1 and 2 respectively correspond to the *x* and *y* directions in the FE model in figure 5.

as sketched in figure 5. Symmetric excitation is applied on both the top and bottom sides of the plate to reduce the signal complexity by considering the primary S0-second harmonic S0 Lamb wave mode pair in the analyses. The size of the PZT actuator is arbitrarily chosen as 8 mm × 0.5 mm. The MF contains ten elements as shown in figure 5. The thickness of the bonding layers in both actuator and MF areas is set to 50 μm.

A series of our previous work demonstrated that the material nonlinearity of the bonding layer under the PZT actuator, referred as adhesive nonlinearity, is a common occurrence which may overwhelm the damage-induced nonlinear wave components if the system is not properly designed [13, 14, 26]. Therefore, adhesive nonlinearity is used as a typical example of deceptive nonlinear source in the system in the subsequent analyses. The damage-related material nonlinearity of the plate and the representative non-damage-related adhesive nonlinearity are therefore considered in finite element model which are both characterized by the Landau–Lifshitz model [14] with the stress–strain relation expressed as

$$\mathbf{T^{RR}} = \lambda tr\,[\mathbf{E}]\,\mathbf{I} + 2\mu\mathbf{E} + \bar{A}\mathbf{E}^2 + \bar{B}tr\,\left[\mathbf{E}^2\right]\mathbf{I}$$
$$+ 2\bar{B}tr\,[\mathbf{E}]\,\mathbf{E} + \bar{C}(tr\,[\mathbf{E}])^2\mathbf{I} \qquad (1)$$

where λ and μ are Lamé constants, which are directly linked to the Young's modulus E, and Poisson's ratio v. $\bar{A}$, $\bar{B}$, $\bar{C}$ are the Landau third-order elastic constants. **I** is the second rank identity tensor and the operation $tr[\ ]$ represents the trace. $\mathbf{T^{RR}}$ denotes the second Piola-Kirchhoff stress tensor. **E** is the Lagrangian strain tensor, which is defined in terms of the displacement gradient, $\mathbf{H} = \nabla\mathbf{u}$, as

$$\mathbf{E} = \frac{1}{2}\left(\mathbf{H} + \mathbf{H^T} + \mathbf{H^T H}\right). \qquad (2)$$

The Landau–Lifshitz model is embedded in the finite element simulations via a user material subroutine (UMAT). The Landau constants of the adhesive and aluminum used in the simulations are listed in table 2 while the detailed parameters for the PZT are listed in table 3 which are identical to those used in our previous work [14]. All physical parameters used in the simulation, are deemed rather realistic, as demonstrated in the same previous paper. It is worth noting that, if the influence of the adhesive nonlinearity at the actuating part could be eliminated by the designed MF, other nonlinear effects from the actuating part can also, in principle, be mitigated since all these nonlinear sources locally generate the deceptive second harmonic wave components at the actuating area. Considering
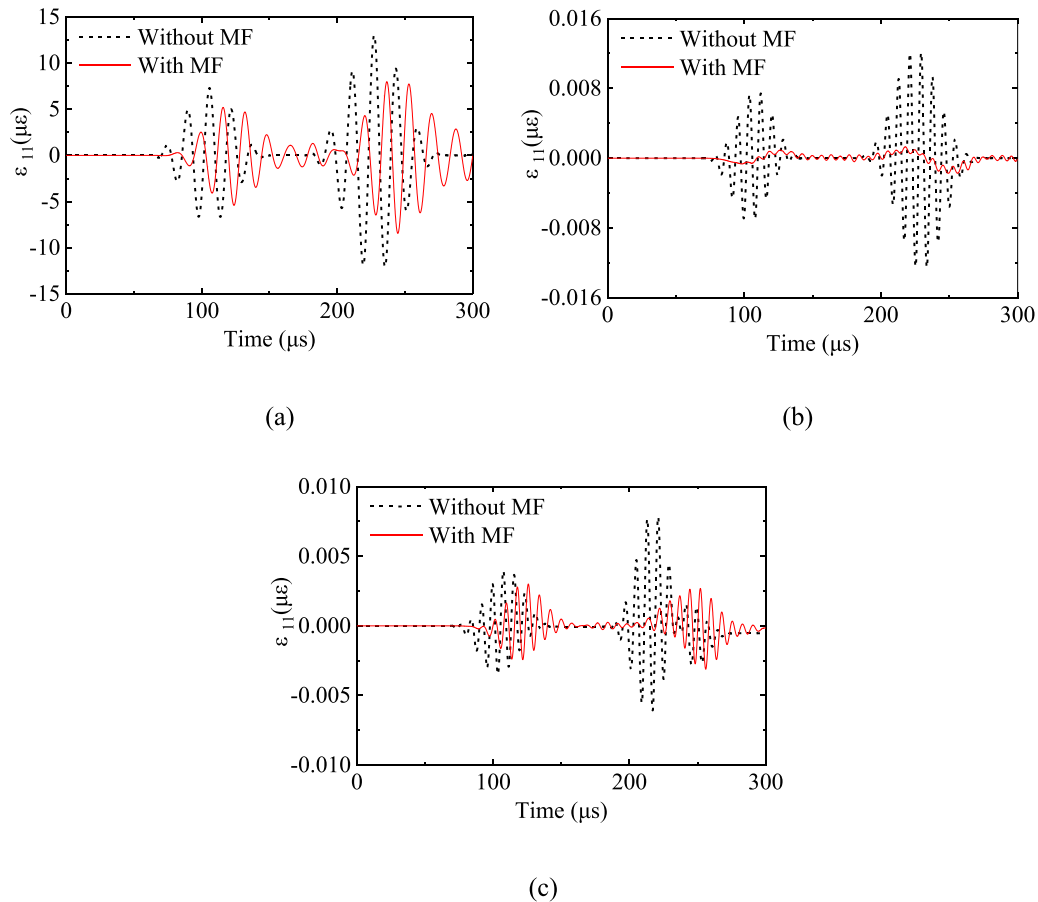
Figure 6. (a) Linear, (b) adhesive-nonlinearity-induced, and (c) material-nonlinearity-induced responses with and without MF under 60 kHz excitation.

the two bandgaps in figure 2(c), two excitation frequencies are selected as 60 kHz and 100 kHz in the low frequency range of interest with their second harmonic frequencies falling into the two bandgaps, respectively. In both cases, a pair of 200 V tone burst excitation signals modulated by Hann window with inversed phases is applied on the PZTs with the fixed time-duration (100 μs). The normal strain (ε_{11}) of the sensing point at 300 mm away from the actuators is extracted as the system response. A superposition method [14] is used to further extract the second harmonic responses in the time-domain by superposing the responses to the two inversed excitations.

Different nonlinear sources are separately considered in simulations to examine how the captured responses are affected by the MFs. First, the 60 kHz excitation case is studied whose second harmonic frequency is located inside the Bragg scattering bandgap. The performance of the designed MFs is evaluated by tactically including and excluding the adhesive nonlinearity and the material nonlinearity of the plate in the finite element model. First, without any nonlinearity in the system, the linear strain responses are compared before and after the installation of the MFs, as shown in figure 6(a). In each signal, the first wave packet corresponds to the direct wave while the second one is from the boundary reflections. Apart from the phase lag, a noticeable reduction in the linear wave amplitude is observed. This is apparently due to the use of MF which

reflects part of the wave energy. However, the impaired level is deemed acceptable. Then the adhesive nonlinearity at both actuator and MF areas is introduced to the model. By superposition the responses to a pair of inverse excitation signals, the second harmonic responses are extracted in the time domain and compared in figure 6(b) with/without MFs. It follows that the deceptive second harmonic response from the adhesive is remarkably mitigated by the designed MFs. Finally, only the material nonlinearity of the plate is included in the simulations and the corresponding second harmonic responses are shown in figure 6(c). It can be seen that, although the amplitude of the nonlinear waves decreases after the installation of the MF, it still has a sufficiently large energy to be detected.

Similar analyses are conducted for 100 kHz excitation case, with results shown in figure 7 for which the second harmonic frequency locates in the locally resonant bandgap. In this case, the linear response is dramatically attenuated by the MFs (figure 7(a)) which results in a significant attenuation in the nonlinear response induced by the material nonlinearity of the plate (figure 7(c)). To make things even worse, the deceptive second harmonic response generated by the adhesive nonlinearity is increased after the installation of the MF (figure 7(b)). Note that as a common practice, the calculation of the band structure discussed in the previous section does not consider the adhesive nonlinearity. Apparently, the
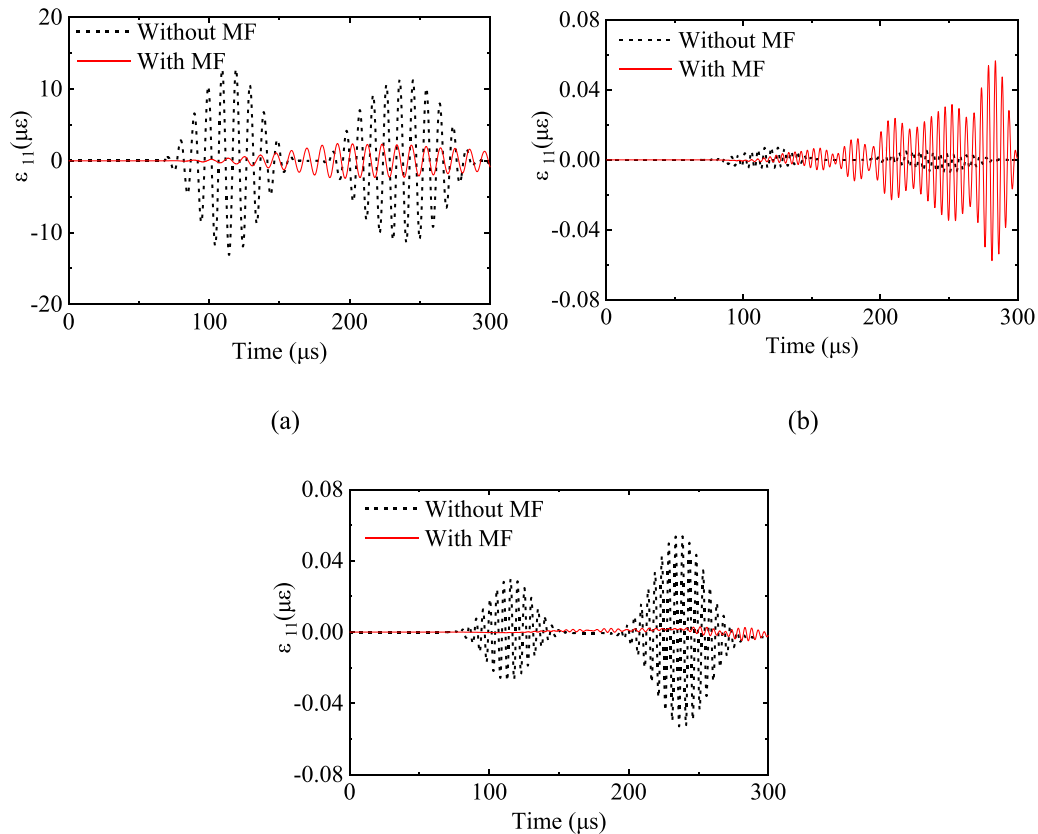
Figure 7. (a) Linear, (b) adhesive-nonlinearity-induced, and (c)material-nonlinearity-induced responses with and without MF under 100 kHz excitation.
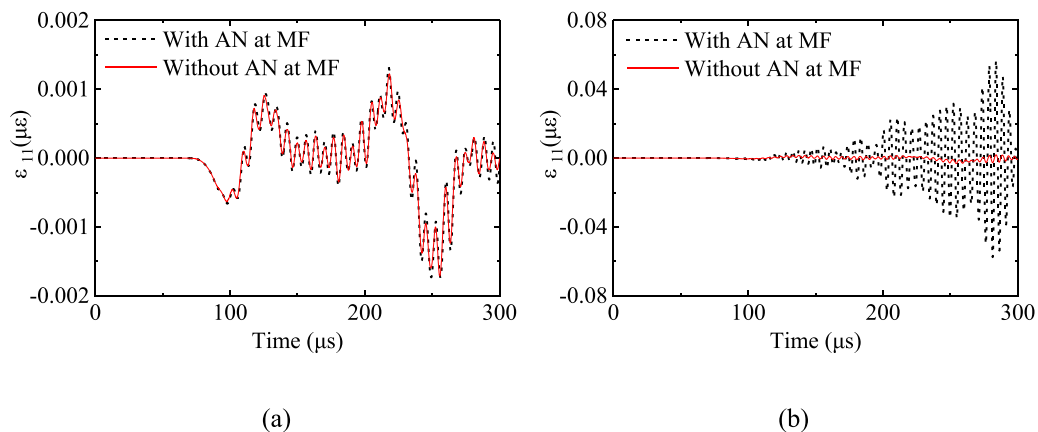
Figure 8. Second harmonic responses with and without adhesive nonlinearity at the MF: (a) 60 kHz excitation case corresponding to Bragg scattering; (b) 100 kHz excitation case corresponding to local resonance.

adhesive nonlinearity plays out more drastically in the frequency range controlled by local resonances. This is understandable since adhesive layers play a more active role in the local deformation when MFs are locally resonant, contrary to the Bragg scattering case which basically relies on wave interference.

To make this clearer, the two cases with different excitation frequencies are examined again by keeping and removing the adhesive nonlinearity only in the MF area. Note in both cases, the adhesive nonlinearity in the actuator is always considered.

Similarly, the second harmonic responses are extracted and shown in figure 8. For 60 kHz excitation case corresponding to the Bragg scattering mechanism (figure 8(a)), the adhesive nonlinearity at the MF area shows negligible influence on the captured nonlinear responses. On the contrary, the 100 kHz excitation case seems to be drastically affected by the adhesive nonlinearity at the MFs, again due to its local resonance nature, as shown in figure 8(b). This again is consistent with the underlying working mechanisms of the two bands. Therefore, the Bragg scattering mechanism shows advantages over
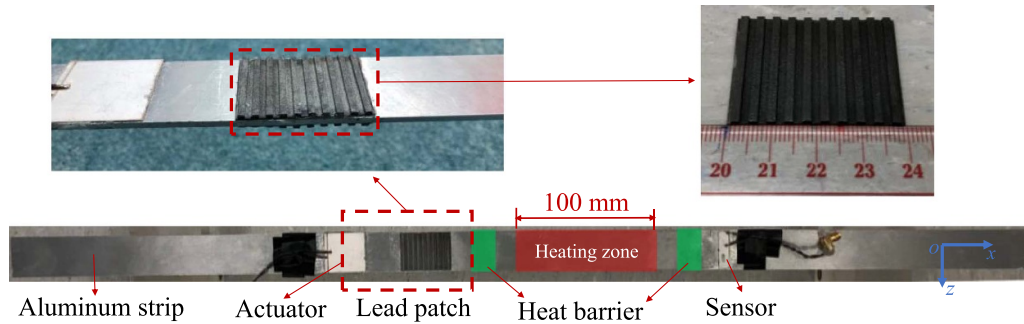
Figure 9. Test specimen.

the locally resonant one owing to its more robust immunity to the nonlinearity introduced by the installation of the MF.

To sum up, the two bandgaps of the designed MF are tested to show their ability to filter out deceptive second harmonic components originating from the actuating area. For the local resonance-induced one, the primary waves are significantly attenuated by the MFs, resulting in a low generation efficiency of the damage-related nonlinear wave components. In addition, due to the local resonance of the MF, its inherent nonlinearity exemplified by the adhesive nonlinearity also generates non-negligible deceptive second harmonic components, which deteriorates the extraction of damage information. By comparison, the designed MF under the Bragg scattering mechanism enables significant mitigation of deceptive second harmonic responses generated by the nonlinear sources at the actuating area. Meanwhile, the adhesive nonlinearity of the MF assembly has a negligible effect on the system performance. Furthermore, it also allows the passing of sufficiently strong linear probing waves for subsequent generation of damage-related nonlinear waves. Therefore, the Bragg scattering induced bandgap is recommended for further NGW-SHM applications.

4. Experimental validations

The designed MF was fabricated, implemented, and experimentally tested for SHM applications. The test specimen is illustrated in figure 9. A 2 mm thick 2024-T3 aluminum strip of 800 mm × 30 mm was inspected. A 30 mm × 30 mm × 0.5 mm PZT actuator was bonded on the strip with UHU 2-component epoxy. A PZT sensor, 8 mm × 30 mm × 0.5 mm, was placed 300 mm away from the actuator. Same as in the numerical simulation, the lead patches contain ten unit cells whose geometric parameters are listed in table 1. The total length of the MF patch was 40 mm. The lead patches were symmetrically bonded on the top and bottom surfaces of the aluminum strip. Measurements were conducted with the National Instrument system as shown in figure 1.

The experimental procedure was as follows. First, the guided wave signals were measured before and after the installation of the MFs on the intact strip to assess its performance before any damage was introduced into the test sample. In light of the band structure analyses and the time-domain

finite element results reported above, a 200 V five-cycle tone burst excitation at 60 kHz was used to match with the Bragg scattering bandgap. Responses from the sensing PZT before and after the installation of the MFs were obtained, as shown in figure 10(a). As mentioned above, it was extremely difficult to attribute the wave packets to different Lamb wave modes due to the reflections from the edges of the strip. Therefore, a long enough signal was recorded to ensure the wealth of damage information contained in the captured guided wave signals. To confirm the wave filtering ability of the designed MF, responses to a 120 kHz excitation inside the predicted bandgap was also measured and shown in figure 10(b). Contrary to the 60 kHz excitation case for which the energy level of the signal is not drastically reduced, the significantly attenuated signal level at 120 kHz confirms the validity of the MF design and expected wave filtering effect.

To further quantify the wave attenuation property of the MFs at different frequencies, an attenuation ratio (AR) is defined as

$$AR = \frac{CA_{\text{with MF}}}{CA_{\text{without MF}}} \tag{3}$$

where CA denotes the characteristic amplitude of a signals, calculated as

$$CA = \sqrt{\int_0^T (x(t))^2 \mathrm{d}t} \tag{4}$$

where $x(t)$ denotes a time-domain signal and T is the total length of the signal. By scrutinizing the responses at different frequencies (from 50 kHz to 250 kHz stepped by 5 kHz), the corresponding ARs are shown in figure 11. The two predicted bandgaps from section 2 are also marked in red strips. It can be seen that most energy can be filtered out at those frequencies roughly falling inside the bandgaps, which proves the effectiveness of the designed MF.

The nonlinear responses for the 60 kHz excitation case are then studied. By conducting the fast Fourier transform (FFT) to the signals in figure 10(a), the spectra of the captured responses are shown in figure 12. Before the installation of the MFs, a second harmonic response peak is obvious. With the MFs, despite a reduction in the linear wave amplitude, as already demonstrated in figure 6(a) and confirmed again here,
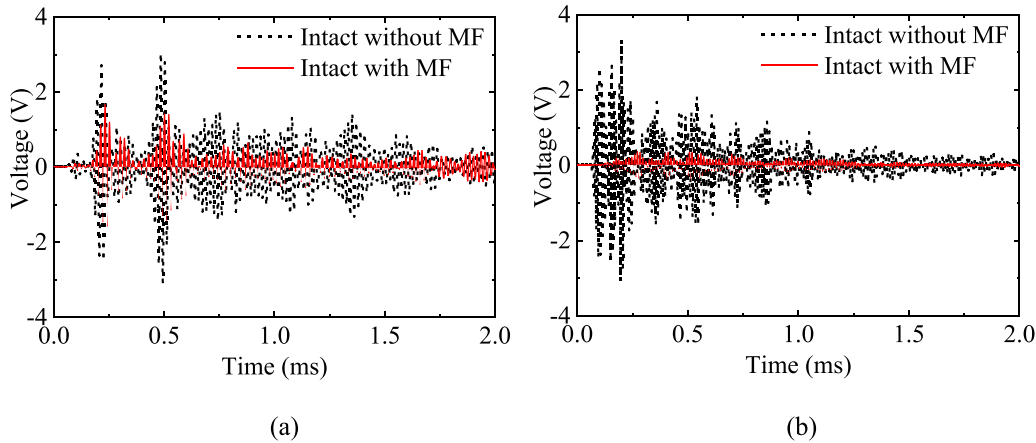
Figure 10. Responses to (a) 60 kHz and (b) 120 kHz excitations in the intact strip before and after the installation of the MF.
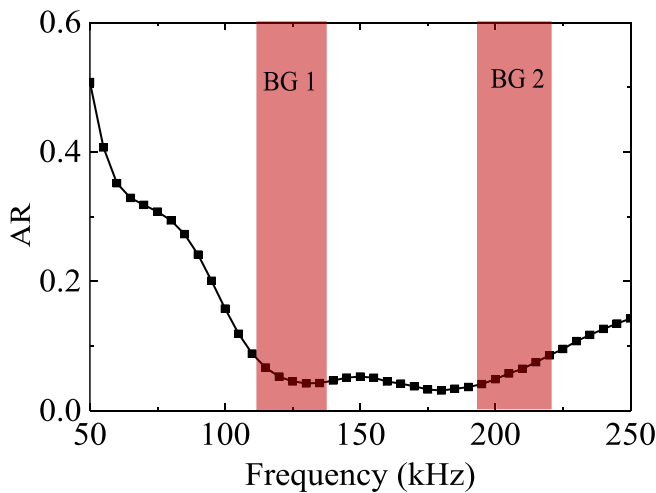
**Figure 11.** Attenuation ratio achieved by the MF at different frequencies.
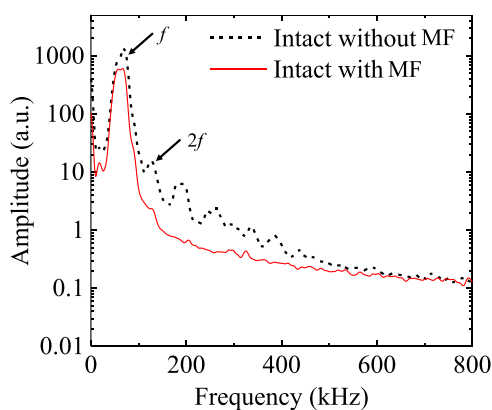
Figure 12. Spectra of the responses to 60 kHz excitation in the intact strip before and after the installation of the MF.

the second harmonic response basically disappear. This observation confirms the successful elimination of the non-damage-related nonlinear components after the deployment of the MFs.

As an SHM example, a thermal ageing treatment was applied to the aluminum strip (figure (9)) to create material microstructural changes in order to mimic a typical incipient damage within a small area. The length of the heating zone was 100 mm and the heating temperature was kept at 400 °C for 3 h with a dedicated heating platform, with details given in [13, 34]. According to our previous work, such a heating scheme can effectively create material microstructural changes, which were also confirmed by Vickers hardness test [34]. Heat barriers around the heating area were installed with flowing water to prevent the heat from reaching the MF and PZT areas. With the aid of the heat barriers, the temperature outside the barriers zones were kept less than 60 °C during the whole heating process, which should have negligible influence on the MF and transducers. Such a practice has been extensively discussed and justified in the literature [35] and in our previous work [13, 34]. It is worth noting that, although it is difficult to quantitatively link such material microstructural changes to an existing type of mechanical incipient damage, one can surmise that once its efficacy is demonstrated using the present example, the method can then be extended to other type of damage such as plasticity- or fatigue-induced microstructural changes.

Measurements were carried out on the heated strip. The responses to the 60 kHz excitation with the MFs before and after heating the strip are compared in figure 13. It can be seen that the overall response was slightly affected after the damage was introduced as shown in figure 13(a). By further examining their spectra after the FFT analysis, a dramatic increase in the second harmonic amplitude can be observed after the plate is heated, as shown in figure 13(b). This proves that the material microstructural changes can be effectively detected in this system, thanks to the effective purification of the nonlinear waves by the MFs.

The MF was then removed, followed by additional ultrasonic measurements on the same heated sample. This allowed a direct comparison between the two cases before and after the material microstructural changes in the absence of the MF. Using 60 kHz excitation, the results are shown in figure 14, in both time and frequency domains. It follows that no

(a)　　　　　　　　　　　　　　　　　　　　　　　　(b)
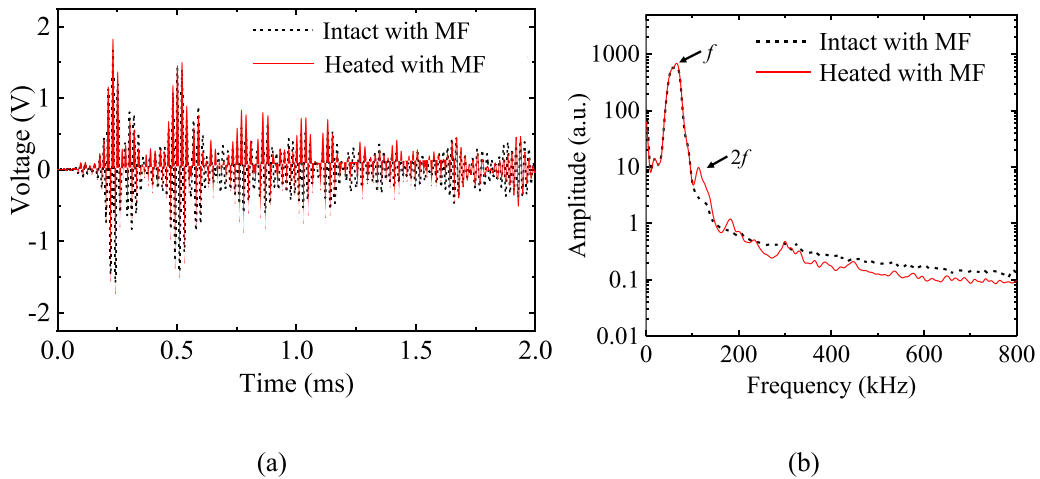
Figure 13. Responses to 60 kHz excitation with MF before and after the strip is heated: (a) time-domain signals; (b) their spectra.

(a)　　　　　　　　　　　　　　　　　　　　　　　　(b)
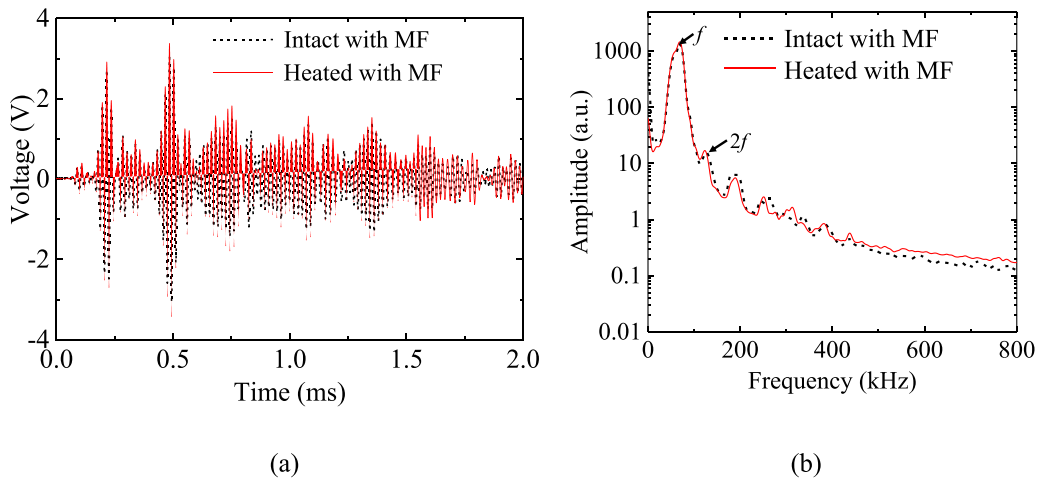
Figure 14. Responses to 60 kHz excitation without MF before and after the place is heated: (a) time-domain signals; (b) their spectra.

(a)　　　　　　　　　　　　　　　　　　　　　　　　(b)
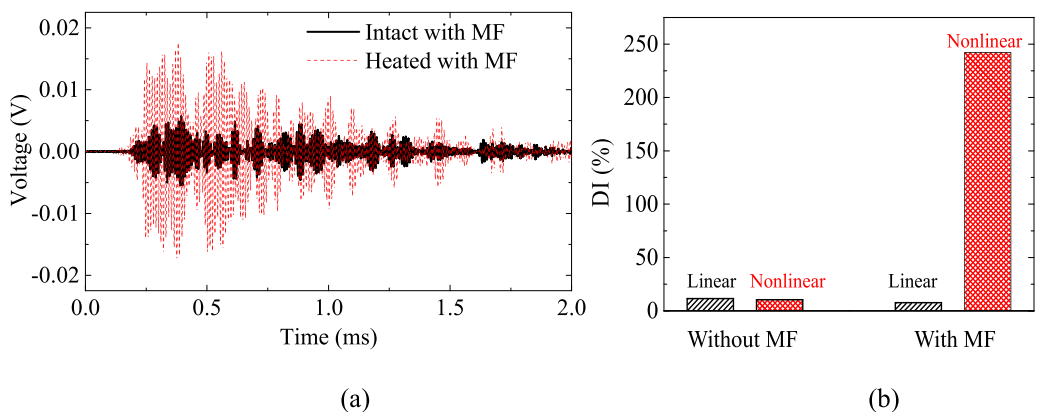
Figure 15. (a) Extracted second harmonic time-domain responses before and after the strip is heated with the MF; (b) DIs calculated with different guide wave components.

meaningful changes can be observed from either the linear or the second harmonic responses. This again confirms the fact that deceptive nonlinear effects dominate in the system, thus overwhelming the material-generated nonlinear components without the MF.

Finally, the efficiency of the material microstructural change detection method using different signal features (linear and nonlinear responses without and with the MF) is quantified. A damage index (DI) is defined using the previously defined characteristic amplitude (equation (4)) as

$$DI = \frac{|CA_{heated} - CA_{intact}|}{CA_{intact}} \times 100\%. \qquad (5)$$

It is worth noting that the calculation of CA for the linear time-domain responses is straightforward. The nonlinear responses should be extracted using a previously developed superposition method [14]. In addition, a Butterworth band-pass filter (90–150 kHz) is applied to reduce the influence of noise. An example of the extracted nonlinear time-domain signals for the intact and heated cases with the MFs in place is shown in figure 15(a). A dramatic increase is observed in the nonlinear wave responses after the strip is heated, which further supports the results in figure 13(b). DIs using different time-domain wave responses are calculated and compared in figure 15(b). It can be seen that, without the MFs, neither linear nor nonlinear wave component is able to detect the material microstructural changes due to the adverse and overwhelming interference from the deceptive nonlinear components in the system. After the MF is installed, although the linear wave is still not sensitive to the material microstructural changes, the nonlinear wave, purified by the designed MF, shows remarkably high sensitivity.

5. Conclusions

This paper proposes the design and implementation of a metamaterial filter (called MF) to facilitate the detection of material microstructural changes in a NGW-based SHM system. As a patch to be surface-mounted on the structure under inspection, the proposed MF is intended to purify the probing waves through the tactical elimination of non-damage-related nonlinear components emitted from the actuation area. The proposed MF assembly (with the adhesive bonding and the host structure) offers bandgaps resulting from Bragg scattering and local resonances. Their respective band features, in terms of bandgap frequency and bandwidth, are investigated through numerical analyses on bonding conditions and symmetry of the metamaterial lattice. Time-domain finite element investigations are carried out to validate the efficacy of the MF. Specifically, as a representative non-damage-related nonlinear source, the adhesive nonlinearity at the MF area is evaluated to reveal its influence on the wave purification efficiency under the two identified bandgap mechanisms. Experiments are finally conducted with the designed MFs. The purified second harmonic Lamb waves are finally applied to detect material microstructural changes induced by a thermal ageing treatment on a metal strip sample.

In principle, both Bragg and local resonance bandgaps can be used for wave filtering purposes. The former requires symmetrical installation of the MF to achieve a relatively wide frequency range for wave filtering. The latter needs precise control of the bonding quality of the MF to ensure the wave filtering consistency. Moreover, the Bragg bandgap outperforms the locally resonant one in terms of robustness and immunity to the nonlinearities of the MF assembly, mainly from the adhesive layers. In light of this and the fact that the bonding thickness is difficult to be precisely controlled when

installing the MF, Bragg scattering-induced bandgap is seen to be a better choice for wave filtering. Experiments demonstrate the effectiveness of the MF in NGW-SHM applications. Without the MF, strong non-damage-related nonlinear components generated around the actuation area are proven to exist in the NGW-SHM system which significantly deteriorate its ability for the detection of microstructural changes. By comparison, with the deployment of the MF, probing waves are purified by filtering out these deceptive nonlinear components. Through the definition of a DI, NGW-SHM is successfully carried out to detect thermal-aging-induced material microstructural changes with extremely high sensitivity compared to the linear-guided-wave-based technique.

The work presented in this paper, through revealing the underlying mechanisms of the MF design and analyzing different influencing factors associated with its implementation, paves the way forward for promising NGW-SHM applications. The MF discussed in this paper is rather primitive involving a simple strip configuration. While this is intended as a proof-of-concept study, other systems such as plates should be further investigated, whichwell-controlled installation of the MF patches to ensure the symmetry of the MF assembly. Nevertheless, the principles being put forward in this paper can be followed, through more sophisticated design methods such as topology optimizations [36, 37], to achieve better or multi-functional wave manipulation devices for various NGW-SHM applications.

ORCID iDs

Shengbo Shan ● https://orcid.org/0000-0002-0950-6193
Li Cheng ● https://orcid.org/0000-0001-6110-8099

References

[1] Giurgiutiu V 2007 *Structural Health Monitoring: With Piezoelectric Wafer Active Sensors* (Amsterdam: Elsevier)
[2] Mitra M and Gopalakrishnan S 2016 Guided wave based structural health monitoring: a review *Smart Mater. Struct.* **25** 053001

[3] Yu L and Tian Z 2013 Lamb wave structural health monitoring using a hybrid PZT-laser vibrometer approach *Struct. Health Monit.* **12** 469–83

[4] Amjad U, Yadav S K and Kundu T 2015 Detection and quantification of pipe damage from change in time of flight and phase *Ultrasonics* **62** 223–36

[5] Su Z, Zhou C, Hong M, Cheng L, Wang Q and Qing X 2014 Acousto-ultrasonics-based fatigue damage characterization: linear versus nonlinear signal features *Mech. Syst. Signal Process.* **45** 225–39

[6] Matlack K H, Kim J-Y, Jacobs L J and Qu J 2015 Review of second harmonic generation measurement techniques for material state determination in metals *J. Nondestruct. Eval.* **34** 273

[7] Matsuda N and Biwa S 2011 Phase and group velocity matching for cumulative harmonic generation in Lamb waves *J. Appl. Phys.* **109** 094903

[8] Deng M 1999 Cumulative second-harmonic generation of Lamb-mode propagation in a solid plate *J. Appl. Phys.* **85** 3051–8

[9] Wan X, Tse P, Xu G, Tao T and Zhang Q 2016 Analytical and numerical studies of approximate phase velocity matching based nonlinear S0 mode Lamb waves for the detection of evenly distributed microstructural changes *Smart Mater. Struct.* **25** 045023

[10] Yang Y, Ng C-T, Kotousov A, Sohn H and Lim H J 2018 Second harmonic generation at fatigue cracks by low-frequency Lamb waves: experimental and numerical studies *Mech. Syst. Signal Process.* **99** 760–73

[11] Pruell C, Kim J-Y, Qu J and Jacobs L J 2007 Evaluation of plasticity driven material damage using Lamb waves *Appl. Phys. Lett.* **91** 231911

[12] Deng M and Pei J 2007 Assessment of accumulated fatigue damage in solid plates using nonlinear Lamb wave approach *Appl. Phys. Lett.* **90** 121902

[13] Shan S, Cheng L and Wen F 2018 Design of nonlinear-Lamb-wave-based structural health monitoring systems with mitigated adhesive nonlinearity *Smart Mater. Struct.* **27** 105006

[14] Shan S, Cheng L and Li P 2016 Adhesive nonlinearity in Lamb-wave-based structural health monitoring systems *Smart Mater. Struct.* **26** 025019

[15] Tian Y, Shen Y, Rao D and Xu W 2019 Metamaterial improved nonlinear ultrasonics for fatigue damage detection *Smart Mater. Struct.* **28** 075038

[16] Zhu R, Liu X, Hu G, Sun C and Huang G 2014 Negative refraction of elastic waves at the deep-subwavelength scale in a single-phase metamaterial *Nat. Commun.* **5** 1–8

[17] Dong H-W, Zhao S-D, Wang Y-S and Zhang C 2017 Topology optimization of anisotropic broadband double-negative elastic metamaterials *J. Mech. Phys. Solids* **105** 54–80

[18] Sridhar A, Liu L, Kouznetsova V and Geers M 2018 Homogenized enriched continuum analysis of acoustic metamaterials with negative stiffness and double negative effects *J. Mech. Phys. Solids* **119** 104–17

[19] Sugino C, Ruzzene M and Erturk A 2018 Merging mechanical and electromechanical bandgaps in locally resonant metamaterials and metastructures *J. Mech. Phys. Solids* **116** 323–33

[20] Nanthakumar S, Zhuang X, Park H S, Nguyen C, Chen Y and Rabczuk T 2019 Inverse design of quantum spin hall-based phononic topological insulators *J. Mech. Phys. Solids* **125** 550–71

[21] Liu X, Hu G, Sun C and Huang G 2011 Wave propagation characterization and design of two-dimensional elastic chiral metacomposite *J. Sound Vib.* **330** 2536–53

[22] Lai Y, Wu Y, Sheng P and Zhang Z-Q 2011 Hybrid elastic solids *Nat. Mater.* **10** 620–4

[23] Yan X, Zhu R, Huang G and Yuan F-G 2013 Focusing guided waves using surface bonded elastic metamaterials *Appl. Phys. Lett.* **103** 121901–5

[24] Ciampa F, Mankar A and Marini A 2017 Phononic crystal waveguide transducers for nonlinear elastic wave sensing *Sci. Rep.* **7** 1–8

[25] Tian Y and Shen Y 2020 Selective guided wave mode transmission enabled by elastic metamaterials *J. Sound Vib.* **485** 115566

[26] Shan S, Cheng L and Wen F 2018 Characterization of nonplanar second harmonic Lamb waves with a refined nonlinear parameter *J. Nondestruct. Eval. Diagn. Progn. Eng. Syst.* **1** 011004

[27] Hussein M I, Leamy M J and Ruzzene M 2014 Dynamics of phononic materials and structures: historical origins, recent progress, and future outlook *Appl. Mech. Rev.* **66** 040802

[28] Huang H and Sun C 2009 Wave attenuation mechanism in an acoustic metamaterial with negative effective mass density *New J. Phys.* **11** 013003

[29] Rupin M, Lemoult F, Lerosey G and Roux P 2014 Experimental demonstration of ordered and disordered multiresonant metamaterials for lamb waves *Phys. Rev. Lett.* **112** 234301

[30] Sharma B and Sun C T 2016 Local resonance and Bragg bandgaps in sandwich beams containing periodically inserted resonators *J. Sound Vib.* **364** 133–46

[31] Mead D 1996 Wave propagation in continuous periodic structures: research contributions from Southampton, 1964–1995 *J. Sound Vib.* **190** 495–524

[32] Rayleigh L 1887 XVII. On the maintenance of vibrations by forces of double frequency, and on the propagation of waves through a medium endowed with a periodic structure *London, Edinburgh Dublin Phil. Mag. J. Sci.* **24** 145–59

[33] Giurgiutiu V 2005 Tuned Lamb wave excitation and detection with piezoelectric wafer active sensors for structural health monitoring *J. Intell. Mater. Syst. Struct.* **16** 291–305

[34] Wen F, Shan S and Cheng L 2021 Third harmonic shear horizontal waves for material degradation monitoring *Struct. Health Monit.* **20** 475–83

[35] Hasanian M and Lissenden C J 2017 Second order harmonic guided wave mutual interactions in plate: vector analysis, numerical simulation, and experimental results *J. Appl. Phys.* **122** 084901

[36] Dong H-W, Zhao S-D, Wei P, Cheng L, Wang Y-S and Zhang C 2019 Systematic design and realization of double-negative acoustic metamaterials by topology optimization *Acta Mater.* **172** 102–20

[37] Dong H-W, Zhao S-D, Wang Y-S, Cheng L and Zhang C 2020 Robust 2D/3D multi-polar acoustic metamaterials with broadband double negativity *J. Mech. Phys. Solids* **137** 103889